Cracking mechanism in a laser powder bed fused cold-work tool steel: The role of residual stresses, microstructure and local elemental concentrations

Jan Platl [a,*], Sabine Bodner [a], Christina Hofer [a], Andreas Landefeld [a], Harald Leitner [b], Christoph Turk [b], Marc-André Nielsen [c], Ali Gökhan Demir [e], Barbara Previtali [e], Jozef Keckes [a,d], Ronald Schnitzer [a]

[a] Department of Materials Science, Montanuniversität Leoben, Leoben, Styria 8700, Austria
[b] voestalpine Böhler Edelstahl GmbH & Co KG, Kapfenberg A-8605, Austria
[c] Institute of Materials Physics, Helmholtz Zentrum Hereon, Geesthacht D-21502, Germany
[d] Erich Schmid Institute of Materials Science, Austrian Academy of Sciences, Leoben A-8700, Austria
[e] Department of Mechanical Engineering, Politecnico di Milano, Milano I-20156, Italy

ARTICLE INFO

ABSTRACT

Laser powder bed fusion (LPBF) facilitates economic advantages by enhancing cutting speeds of tools through the implementation of complex internal cooling channels that could not be fabricated otherwise. However, tool steels are prone to cracking during the cyclic remelting process with extremely fast cooling rates due to their high carbon and alloying element contents and related stresses. In this work, a correlation between microscopic crack patterns in a tool steel processed via LPBF, residual stress gradients, local microstructure and near-crack elemental concentrations is studied using longitudinal/transverse sectional synchrotron X-ray micro-diffraction, electron microscopy techniques and atom probe tomography. A formation of horizontal micro-cracks correlates with longitudinal/transverse sectional residual stress drops, especially at geometrically notched positions and sample edges. Remarkably, the cracks propagate predominantly along the network of eutectic intergranular carbides of type M_2C deposited at the grain boundaries of carbon martensite and retained austenite matrix. A comparison of representative carbide sizes at the crack surfaces and within the crack-free regions indicates that cracks propagate preferably through the carbides in a transcrystalline manner, whereas no correlation between the cracking and the martensite formation is observed. The observations link the crack propagation to the solidification microstructure and the prevailing eutectic network. Therefore, the stress-induced cracking of eutectic carbides, which formed during the solidification and fracture in the solid state due to tensile stress accumulations, was found as the predominant cracking mechanism of the tool steel during the LPBF process.

1. Introduction

Owing to its almost unrestricted design freedom, additive manufacturing (AM) facilitates the fabrication of geometrically complex parts that can neither be manufactured with subtractive methods (i.e., turning, milling or drilling) nor with conventional casting. According to a 3D model, material is consolidated most commonly in a layerwise manner during AM. This enables an implementation of novel geometrical features like cooling channels and complex surfaces. The most widely used AM processes for metals are directed energy deposition (DED) and powder bed fusion (PBF) based processes. Compared to the DED processes, the PBF techniques are better suited to the production of small to medium-sized parts with more complex geometries and higher accuracy due to a reduced layer thickness and smaller beam size. Laser powder bed fusion (LPBF) is arguably the most flexible PBF technique based on optical absorption of the energetic beam, which is more easily

* Corresponding author.
  E-mail address: jan.platl@unileoben.ac.at (J. Platl).

adapted to novel alloys. Alongside these beneficial impacts, LPBF is restricted to small parts and production volumes due to low build-up rates [1–4].

A promising application field of LPBF is the tooling industry. With regard to cutting applications, drills or milling cutters made of high-speed steels (HSS) with integrated cooling channels [5] could improve the efficiency by higher cutting velocities compared to conventionally manufactured HSS, which lack of these complex internal structures. The process of LPBF also facilitates the near-net shaped production of cold-work tools. This yields a significant reduction of the post-processing effort for tools that are for example utilized in stamping, coinage or punching applications. For hot-work tool steels, the implementation of conformal cooling channels can lead to shorter cycle times and better thermal control for injection molding applications [6].

In general, already known phenomena from classical casting or welding can be taken into account to better understand failure mechanisms of metals with poor processability during AM. Besides cold cracking, certain metals such as stainless steels, Al-based and Ni-based alloys are susceptible to cracking during solidification [7]. These cracks basically form due to solidification shrinkage and thermal contraction during cooling. In addition, thermal stresses that are often caused by the nature of the fabrication process contribute to crack formation in the semisolid region (also known as mushy zone). In casting, this type of cracks is called hot-tearing [8], whereas in welding, this phenomenon is known as solidification cracking [9]. According to the hot-tearing model for columnar dendritic solidification of metallic alloys proposed by Rappaz et al. [10], tensile stresses cause the formation of so-called hot tears in the mushy zone, if the flow of liquid material is insufficient. With regard to LPBF, hot-tearing has been observed for high-entropy alloys (HEA). Sun et al. [11] concluded the presence of intergranular solidification cracks regardless of the used processing parameters in a CoCrFeNi HEA. Those cracks are caused by large residual stresses due to coarse grains as no elemental segregations were determined at grain boundaries. Further investigations dealing with minor Al additions of 0.5 at% to this HEA [12] revealed the potential of segregation engineering in order to drastically reduce hot-tearing due to prevention of liquid films in interdendritic regions. However, it should be noted that already an addition of 1 at% of Al yielded the presence of intragranular cold cracks. In addition, Zhang et al. [13] investigated an equiatomic CoCrFeMnNi HEA and found that cracks exhibit features of hot-tearing as well as of cold cracking. Similar findings were already published by Tomus et al. [14], who investigated a LPBF Ni-based alloy (Hastelloy-X). They concluded that cracks form during solidification but then propagate due to thermal cycling in the solid state. The elements C and Si were found to strongly influence crack initiation by increasing the hot-tearing sensitivity. For another LPBF Ni-based superalloy (IN738LC), also solidification cracking was assigned as predominant cracking mechanism by Cloots et al. [15]. Zr-rich segregations at grain boundaries were determined as possible reason for the crack initiation. In summary, HEAs and Ni-based superalloys processed with LPBF are vulnerable to hot-tearing respectively solidification cracking. Many influencing factors such as grain size, residual stresses, grain boundary segregations or the presence of liquid films on grain boundaries during solidification play a crucial role in the severity of this susceptibility.

In recent years, a lot of research on carbon-free steel grades, i.e., 17-4PH, 15-5PH and 18Ni300 maraging steel, which promise good processability using LPBF, has been conducted. Papers dealing with the influence of process parameters on part density and hardness [16] or the impact of post-process heat treatment on mechanical and corrosive properties [17] were published. In contrast to conventional carbon-containing tool steels, maraging steels basically gain their hardness by the precipitation of intermetal-

lic phases from a soft nickel martensite [18–20] instead of forming secondary hardening carbides in a matrix of carbon martensite and retained austenite. High hardness can be achieved after direct aging or tempering of as-built parts. This is guaranteed by the high supersaturation due to rapid cooling processes after LPBF. Hadadzadeh et al. [21] investigated a directly-aged FeCrNiAl maraging stainless steel after LPBF and measured a microhardness of ~500 $HV_{0.3}$. Even higher hardness of almost 650 HV (58 HRC) has been reported by Yasa et al. [22] on directly-aged (480°C for 5 h) 18-Ni300 maraging steel after LPBF in comparison to conventionally manufactured and fully heat-treated (solution annealing and aging) counterparts, obtaining only a hardness of 52 HRC. For carbon-containing tool steel grades, after direct tempering at 550°C of a LPBF H13 (~X40CrMoV5-1) hot-work tool steel, Deirmina et al. [23] reported a hardness above 650 HV_1 compared to spark plasma sintered, quenched and tempered H13 with a peak hardness at 500°C of approximately 600 HV_1. However, further increase of wear resistance and hardness is mandatory for highly abrasive cutting applications (i.e., milling, turning and drilling). These requirements are guaranteed by higher carbide contents in HSS or cold-work tool steels only.

On the other hand, certain problems arise during LPBF of the tailored alloying systems of these carbon-containing tool steels. Besides pore formation in alloyed steels, severe cracking may occur in these steels during processing. The former is mainly determined by the applied laser process parameters [24], typically related to the energy density, but also by the incorporated alloying elements [25]. In terms of cracking, recently published papers dealing with LPBF of carbon-containing tool steels [26–28] reported the formation of cold cracks due to a combination of susceptible materials with high carbon equivalent numbers and process-related stresses, which are formed during the complex thermal cycle of the manufacturing process. Crack formation of LPBF tool steels is connected to thermal and consequently residual stresses that evolve during the melting process with very fast cooling rates similar to a microweld. These stresses can be basically attributed to three main sources. Firstly, stresses evolve due to the high thermal gradient caused by a spatially localized laser energy input on a, compared to the focus diameter of the laser source and the melt pool dimension, large area of surrounding colder material represented by the already built part. Although the powder bed and the base plate can be preheated in conventional LPBF systems, the temperatures remain limited (~200°C) with heating efficacy from the bottom reduced as the part grows [29]. Secondly, stresses are brought into the material by the volume reduction during solidification of the melt and by thermal stresses during cooling of the solidified material. Lastly, the formation of hard and therefore brittle carbon martensite could also play a significant role during crack initiation. This transformation from austenite to martensite comes along with a volume expansion incorporating additional stresses into the material [30]. Several publications dealt with the influence of base plate preheating in order to suppress the martensite formation [31,32] and to reduce the process-related thermal stresses by decreasing the thermal gradient [26–28,33–35]. Basically, the risk for crack formation by these two factors was found to be decreased by applying base plate preheating during LPBF. Due to these three stress sources, a complex stress state, which obviously influences the potential crack formation behavior of carbon-containing tool steels during LPBF, can be expected in the part after the LPBF process.

Although remarkable progress has been made in understanding defect formation during AM of metals, the phenomenon of crack initiation and propagation in a carbon-containing tool steel during LPBF, manufactured without preheating the base plate, still remains unclear. The present study hence aims to evaluate the abovedescribed complex stress state in detail and to reveal poten-

tial correlations to crack formation. Therefore, stress evolution in dependence of the part height was determined using high-energy synchrotron X-ray diffraction (HEXRD). These residual stress profiles are correlated to the positions of the cracks, which were visualized on the particular metallographic longitudinal/transverse sections, i.e., on the plane oriented parallely to the build direction. In order to classify the predominant cracking mechanism, detailed investigations of the crack surface morphology and the immediate crack proximity were performed by means of scanning electron microscopy (SEM). In addition, the chemical composition underneath crack surfaces was analyzed using energy dispersive X-ray spectroscopy (EDX) and atom probe tomography (APT). Furthermore, transmission electron microscopy (TEM) diffraction was utilized to determine the crystal structure of microstructural constituents that are incorporated in cracking. The results are combined to propose a theory for the crack formation and propagation mechanism of the investigated carbon-containing cold-work tool steel.

2. Experimental

2.1. Powder and LPBF processing

As feedstock for the LPBF process, spherical cold-work tool steel powder (d10 = 23.0 μm, d50 = 32.9 μm, d90 = 41.7 μm) was used. The powder was produced by Argon gas atomization and subsequently sieved. Its chemical composition (wt%) is 0.85C-0.53Si-0.36Mn-0.19Ni-4.25Cr-2.46W-2.72Mo-2.01V-4.35Co and was determined using inductively coupled plasma optical emission spectroscopy. All investigations performed in the present work were conducted on four samples in the as-built state representing the condition directly after the LPBF process without further post processing. These samples with a base area of 10 × 10 mm² and their respective heights, which are determined by their amount of layers N = 50, 100, 500 and 1000 (layer thickness $D = 30\ \mu m$), were manufactured with a Renishaw AM250 machine and a reduced build volume base plate without a preheating unit on a conventionally manufactured base plate material with a similar composition as the used powder. No support structures were used as the samples were built directly on the base plate. In the following, the samples are designated according to their layer number as sampleN (i.e., sample50, sample100, sample500 and sample1000). The used device is equipped with a fiber laser (75 μm focal diameter at the powder bed height), which operates in pulsed wave emission regime and the sample fabrication was conducted in an Argon gas atmosphere with a maximum oxygen content of 0.1%. As process parameters, the maximum machine power $P = 200$ W, a pulse duration $t = 80\ \mu s$, a point distance $d_p = 88\ \mu m$ and a hatching distance $h = 90\ \mu m$ were chosen. Hence, the laser energy input, which can be calculated as the volumetric energy density $VED = \frac{P \cdot t}{d_p \cdot h \cdot D}$ [36], amounts to 67 J/mm³. Based on previous investigations [37] on the influence of the VED on defect formation of the same material, this parameter set is used as it yields a moderate porosity level. It should be noted that further parameter optimization may lead to lower porosity levels. A meander scan strategy was used, while the scan direction was rotated by 67° after each layer.

2.2. Synchrotron strain profile determination and correlation to metallographic longitudinal/transverse sections

A schematic setup for the longitudinal/transverse sectional synchrotron X-ray micro-diffraction experiment is presented in Fig. 1. Measurements were carried out at the Helmholtz-Zentrum Hereon operated High Energy Materials Science beamline (HEMS) P07B

[38] at the storage ring PETRA III in Hamburg (D). Sample50 and sample100 were scanned along their build direction at two lateral positions using a scanning increment of 20 μm: (i) in the center (center scan) of the sample and (ii) at the edge of the sample (edge scan) in transmission diffraction geometry. Beam's dimensions and energy were set to 500 × 20 μm² ($x \times z$) and 87.1 keV, respectively. Platelets with a thickness of ∼2 mm in the beam direction were extracted from the initial AM cuboids by precision cutting with a Struers Accutom cut-off machine. It follows that two-dimensional (2D) XRD patterns, that were collected by a digital X-ray flat panel detector (type XRD 1621, PerkinElmer; pixel size 200 × 200 μm² in a 2048 × 2048 matrix), represent an average information from diffracting grains within the gauge volume (Fig. 1). A LaB$_6$ standard was used to calibrate the distance of ∼1324 mm between the sample and the detector.

The collected diffraction patterns were further treated using the Python library PyFAI [39]. Each 2D diffractogram was radially integrated to obtain 36 intensity profiles as a function of the Bragg's angle $I(\theta)$, each one representing diffraction data from a detector azimuthal segment of $\Delta \delta = 10$ degrees and the particular sample position (x, z). Subsequently, azimuthally-depended lattice parameters $d_\delta^{hkl}(x, z)$ were determined using the Bragg's law from martensite 112/211 doublet and the austenite 311 peaks, which were fitted using a Pseudo-Voigt function. Azimuthal dependencies of the lattice parameters $d_\delta^{hkl}(x, z)$, which represent elliptical distortions of the Debye-Scherrer rings, can be directly correlated with X-ray elastic strains and residual stresses of the first order within the AM samples. Since the main axes of the elliptical Debye-Scherrer rings were oriented vertically and horizontally (parallel to x and z direction in Fig. 1), it was supposed that shear strain and stresses can be neglected for simplicity.

In case of the center scan, the measured distortion of the Debye-Scherrer rings is proportional to the difference in the in-plane and out-of-plane first order residual stresses $\sigma_{xx} - \sigma_{zz}$, whereby the σ_{zz} component is equal zero at the sample's top surface. For the edge scan, the measured distortion is proportional to the difference in the out-of-plane and in-plane first order residual stresses $\sigma_{zz} - \sigma_{xx}$, whereby the σ_{xx} component is practically negligible at the buildup edge and the distortion recorded during edge scans can be correlated just with the magnitude of the out-of-plane stress σ_{zz}. Importantly, stress values from both scans $\sigma_{xx} - \sigma_{zz}$ and $\sigma_{zz} - \sigma_{xx}$ represent stresses acting along x and z directions, respectively.

The stresses were evaluated by applying the $\sin^2 \psi$-method and X-ray elastic constants (XECs) $\frac{1}{2} S_2^{112/211} = 6.304 \times 10^6$ and $\frac{1}{2} S_2^{311} = 6.535 \times 10^6$ MPa^{-1} for martensite and austenite, respectively. The XECs were estimated from single-crystal constants [40,41] applying the self-consistent Eshelby-Kroener grain interaction model [42]. The evaluation procedure is described in detail in Refs. [43–45]. Residual stress values $\sigma_{xx}(z) - \sigma_{zz}(z)$ and $\sigma_{zz}(z) - \sigma_{xx}(z)$ are presented together with the corresponding X-ray elastic strains $\varepsilon_{xx}^{hkl}(z) - \varepsilon_{zz}^{hkl}(z)$ and $\varepsilon_{zz}^{hkl}(z) - \varepsilon_{xx}^{hkl}(z)$ for both scans, respectively, in Fig. 4, and will be further denoted as stresses and strains, respectively. To reconstruct the stress gradients within the samples before the cutting, a finite element model presented in Ref. [46] was considered.

In order to correlate the residual stress profiles with the samples' morphology, sample50 and sample100 were investigated upon metallographic longitudinal/transverse sectioning. The samples were ground and polished down to 1 μm diamond polishing suspension with a subsequent mechanical polishing step using Struers oxide polishing suspension (OPS). Light optical microscopy (LOM, ZEISS Axio Imager M1m) in unetched and diluted WII solution etched condition was performed from both directions (x and y in Fig. 1 and Fig. 2 (a)) with respect to the build direction z of the LPBF process.
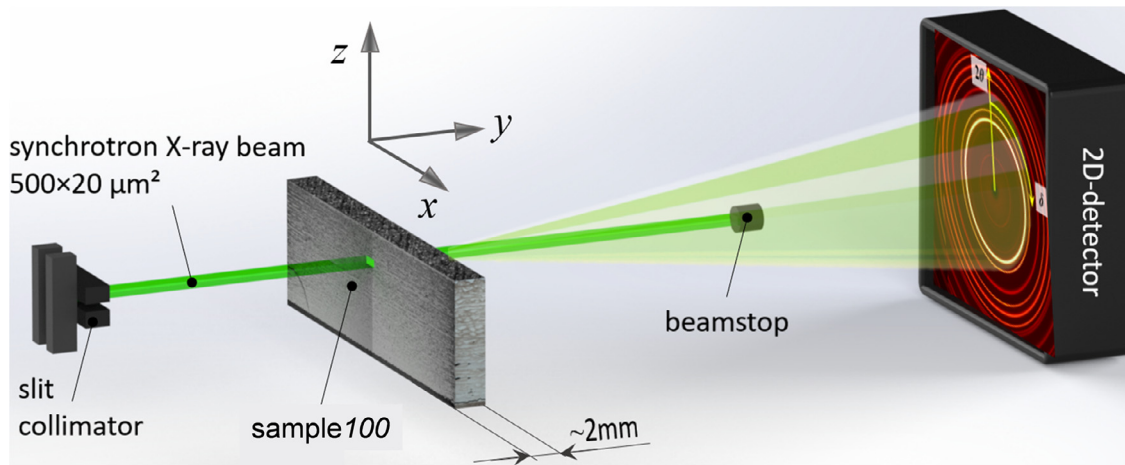
Fig. 1. Scheme of the HEXRD setup exemplarily depicted for sample100.

2.3. Crack surface characterization using SEM

Fig. 2 (a) shows a macroscopic overview of sample*500* (height~15 mm) on which all the following crack surface characterization experiments were performed. Macroscopic crack evaluation was carried out using a Zeiss Discovery.V20 stereo microscope. Special attention was paid to the interface between the base plate and the AM material, which is marked by the white arrow in Fig. 2 (a). Thus, a longitudinal/transverse sectional polish (*x-z* orientation) was investigated in backscattered electron (BSE) mode at a working distance of 8 mm with a Tescan Clara SEM after OPS treatment as described for the LOM investigation above. Unfortunately, cracks in the as-built samples directly after the LPBF process exhibit crack surface areas that are oxidized. In order to account for these oxidation processes and to be able to assess the actual crack surface, a fracture was forced in the upper area of the sample, where no cracks were present after the fabrication process. The fracture surface was immediately analyzed in a SEM (Zeiss GeminiSEM 450) in secondary electron (SE) mode at a working distance of 4 mm and an acceleration voltage of 3 kV after the forced crack opening. The crack opening procedure was performed using a pliers at room temperature after the area of interest was selectively cut free, as shown in Fig. 2 (b). The necessary force to break the sample was applied in negative *z* direction to prevent rubbing of the fracture surfaces. In addition, a qualitative EDX mapping was carried out using a windowless detector (Oxford Instruments, Ultim Extreme) at a working distance of 8 mm. This detector is used to achieve high spatial resolution (sub 10 nm at 2 kV in bulk samples according to [47]) at low energy performance (i.e., 3 kV in the present study at a sample current of 2 nA). A testing time of 3 ms/frame has been chosen and data processing was performed with AZtecLive software.

2.4. Atom Probe Tomography and Transmission Electron Microscopy

APT investigations were performed to characterize the chemical composition of phases, which are present on the crack surface. To ensure that the investigated APT tips stem directly from the crack surface, it was coated with an Ag layer. This layer was deposited in a laboratory-scale unbalanced DC magnetron sputter system from an Ag target (dimensions: Ø50.8 × 6 mm³, 99.99% purity). Ag coating was chosen because of the lower evaporation field of Ag^+ compared to Fe^{++} and Pt^{++} [48], which is necessary to perform APT

measurements, and the absence of peak overlaps (cf. APT sample preparation procedure described in Ref. [49]). In addition to the Ag layer, the area of interest that is located directly next to the transition zone from the base plate to the AM material from which the crack propagation initiates, was protected with a Pt layer, see Fig. 3 (a). The following lift-out procedure including APT tip preparation was carried out using a dual-beam SEM-FIB (focused ion beam) Versa 3D from Thermo Fisher Scientific. Fig. 3 (b) depicts an exemplary APT tip from the Pt coated area after coarse milling with Ga ions at 30 kV. The tip after the final milling step, which intends to remove the entire Pt coating but preserve a small residual amount of Ag, can be seen in Fig. 3 (c). To reduce Ga contamination, this fabrication step was conducted at 5 kV.

To be able to compare the phase evolution on the crack surface to microstructural constituents in crack-free sample areas, further tips were electrolytically prepared using the two step technique in perchloric acetic acid [50] from rectangular rods (~0.3 × 0.3 × 10 mm³) taken from tempered layers of sample*1000*.

All APT measurements were conducted at a temperature of 60 K in a local electrode atom probe (Cameca LEAP 3000X HR) in laser mode at a laser energy of 0.6 nJ. For the electrolytically prepared tips, a pulse frequency of 250 kHz and a target evaporation rate of 1.0% were chosen. As Ag is a heavy element, which is associated with long flight times, a reduced pulse frequency of 160 kHz and an evaporation rate of 0.5% were chosen for tips taken from the crack surface using FIB preparation. Data processing was performed with Imago Visualization and Analysis Software (IVAS version 3.6.14).

Dimensions in APT data are strongly influenced by the reconstruction parameters. Voltage based 3D reconstruction is amongst others dependent on the field factor (k_f), the image compression factor (ICF), the evaporation field of the incorporated elements and the tip geometry [50]. As no pole structures were observed or correlative TEM investigations of the tips were carried out, which can be used to calibrate the reconstruction, a field factor range ($2 < k_f < 8$) was analyzed to account for the potential dimensional changes caused by these impact factors. This range was chosen based on typical k_f values published in Refs [51–54] to qualitatively compare the mean widths of microstructural constituents taken from different sample areas. For the depicted results within this work, the default values provided by the software (ICF=1.65 and k_f=3.30) were used for the electropolished specimen tips. In contrast, a lower field factor (k_f=3.00) was chosen for the FIB-
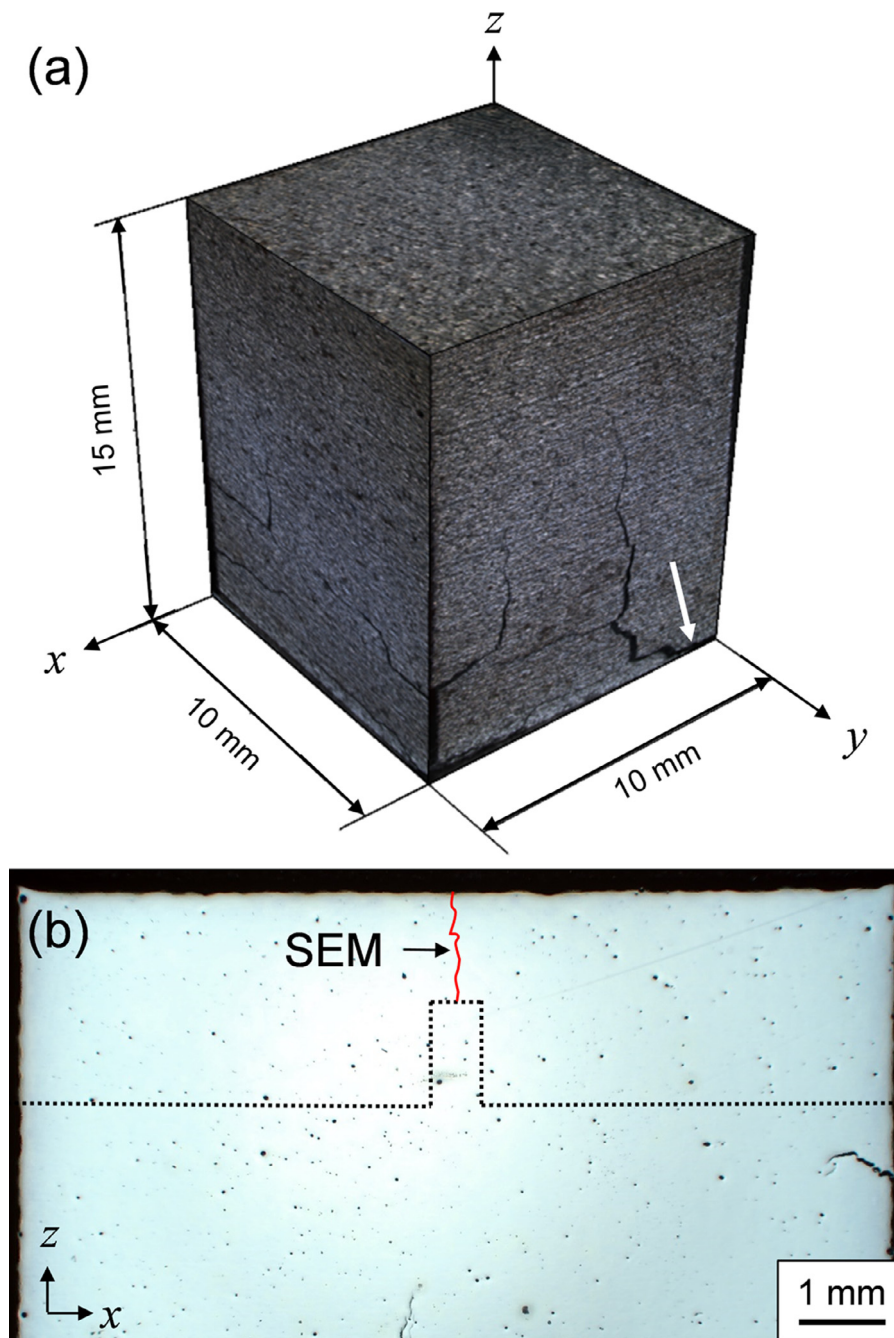
Fig. 2. (a) Macroscopic overview of sample500; (b) illustration of forced crack opening procedure at a crack-free area in the upper sample region of sample500.

prepared tips, which were mounted to a microtip coupon. This decrease in k_f can mainly be attributed to an enhanced electric field caused by the geometry of the microtips [55].

As APT only reveals the chemical composition of microstructural constituents, which are involved in cracking, TEM investigations were performed in order to determine their crystal structure. Therefore, a TEM lamella was prepared using the same dual beam SEM-FIB as for the APT tip preparation. Again, this lamella was taken from the delamination zone at the base plate interface of sample500 (see arrow in Fig. 2 (a)), which was in this case solely protected with a Pt layer. TEM experiments were performed on a Jeol JEM-2200FS TEM equipped with a 200 kV field emission gun. Data processing was carried out with DigitalMicrograph® software (version 3.22.1461.0).

3. Results

3.1. Residual strains/stresses and correlative metallographic longitudinal/transverse sectional analysis

Synchrotron radiation was used to evaluate residual strain $\varepsilon_{xx}^{hkl}(z) - \varepsilon_{zz}^{hkl}(z)$ and $\varepsilon_{zz}^{hkl}(z) - \varepsilon_{xx}^{hkl}(z)$ as well as stress $\sigma_{xx}(z)\sigma_{zz}(z)$ and $\sigma_{zz}(z) - \sigma_{xx}(z)$ profiles at the sample center and the edge, respectively, across two samples with different heights of $\sim$1.4 mm (sample50) and $\sim$2.8 mm (sample100). Phase analysis based on HEXRD measurements of the investigated samples within this work (i.e., sample50, sample100 and sample500) yielded that martensite and austenite amount to more than 90%. Therefore, and also due to the lack of elastic constants for carbides,
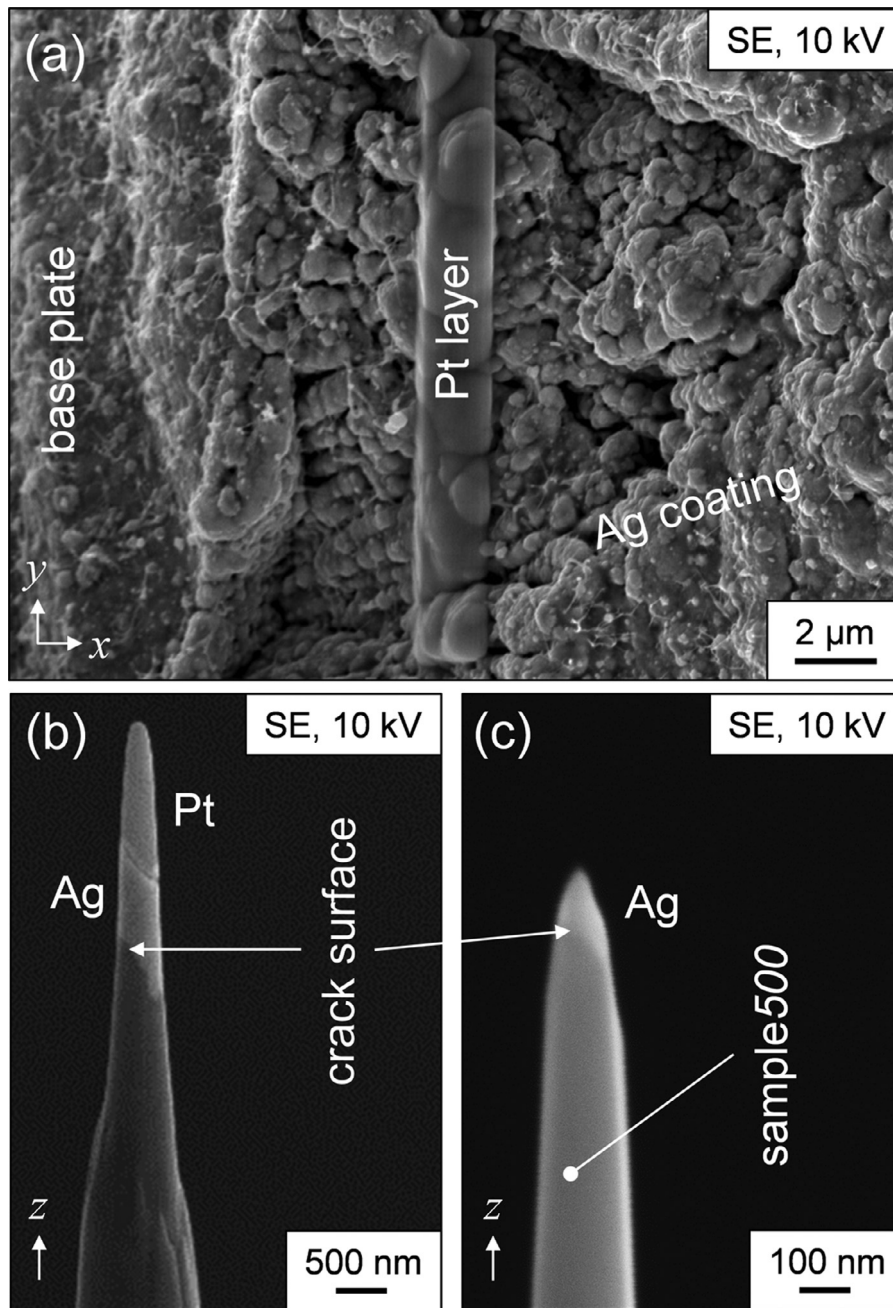
Fig. 3. (a) Ag coated crack surface with protective Pt layer for subsequent APT tip preparation; exemplary APT tip including the crack surface taken from the transition zone after (b) coarse and (c) final ion milling.

strain evaluation was restricted to these two main microstructural constituents.

In Fig. 4 (a), (c) and (f), gray-highlighted planes indicate sample faces, from which the particular LOM micrographs were taken. Fig. 4 (a) depicts almost homogeneously distributed pores on the longitudinal/transverse sectional LOM micrograph, apart from the right specimen edge area, where a pore accumulation can be observed. This pore accumulation can probably be explained by local keyhole collapse around the end of the scan lines resulting in spherical pores. Besides severe cracking at the left sample edge, significant delamination that extends over the whole scan area can be seen in the right transition zone between AM material and base plate, as indicated by the blue arrow in the right lower corner in Fig. 4 (a) and (c). Fig. 4 (b) and (d) show the resulting profiles in which the measured strains are depicted in dependence

of the distance to the top layer for the sample*100* center and its edge, respectively. The former shows a change from high compressive strain of ~1.9‰ for the martensite (depicted in blue) in the top layers to low strain values in the tensile and compression regime for the rest of the AM sample. For the austenite (depicted in green), the top layers also exhibit compressive strains, which are, however, significantly reduced compared to those measured for the martensite. Furthermore, tensile strains could be determined in the austenite in the underlying tempered layers at greater depths throughout the whole longitudinal/transverse section. Strain for the austenite phase in the region of the base plate could not be determined, as the soft-annealed material of the base plate does not contain any austenite.

Compared to the center scan shown in Fig. 4 (b), strain profiles of the edge scan (Fig. 4 (d)), representing $\varepsilon_{zz}^{hkl}(z)$ - $\varepsilon_{xx}^{hkl}(z)$, ex-
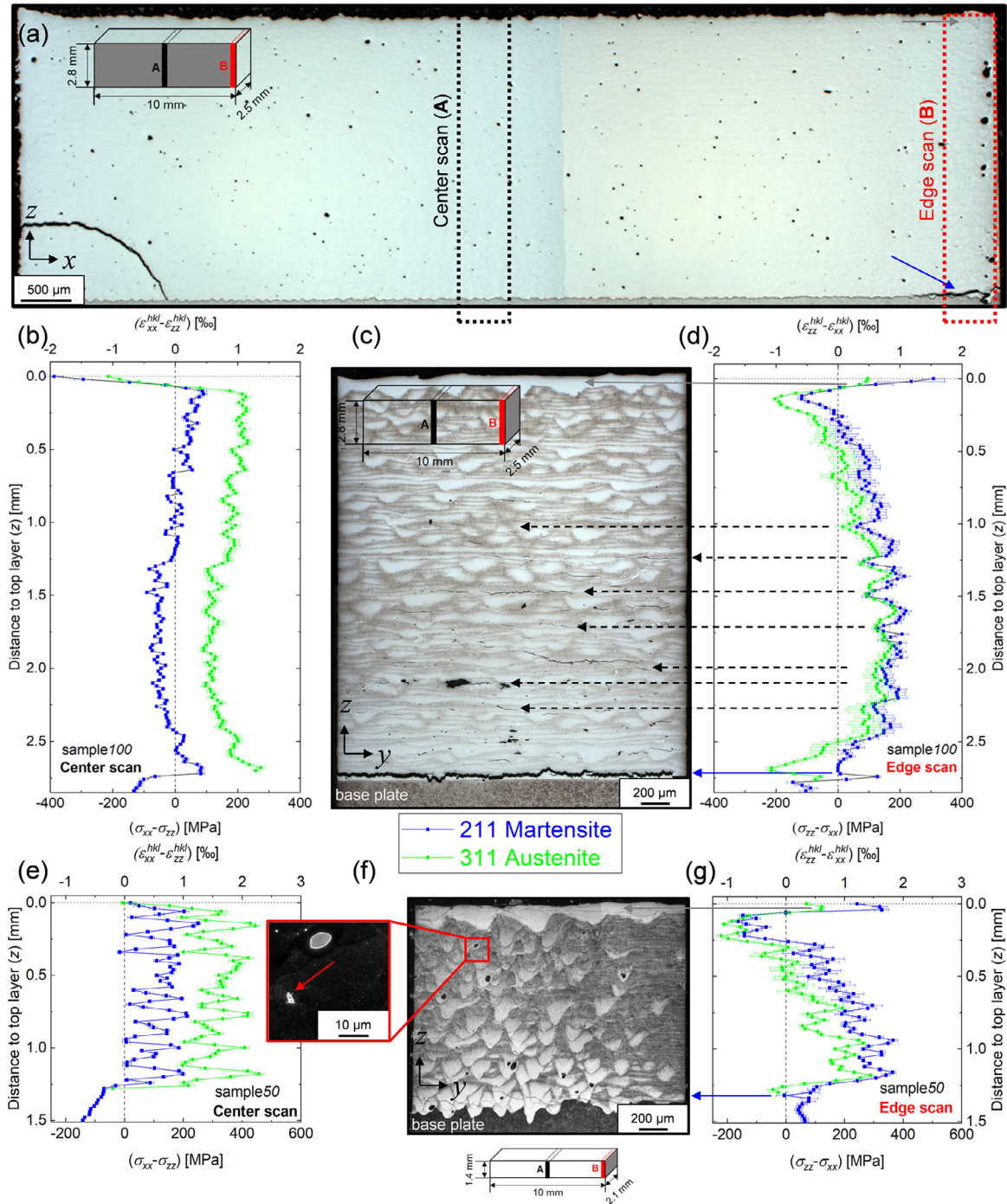
Fig. 4. (a) LOM longitudinal/transverse section (sample100) in unetched condition; (b) strain profile in the sample center; (c) etched LOM longitudinal/transverse section (d) strain profile at the sample edge; (e, g) strain profiles (sample50) in the center and at the sample edge, respectively; (f) corresponding dark-field LOM longitudinal/transverse section with detailed inset of a microcrack. The sketches in (a), (c) and (f) mark the sample investigation direction (highlighted in gray). The gray arrows in (c, d) and (f, g) indicate the different etching attack in top layers, the black dashed arrows correlate crack positions to strain relaxations and the blue arrows mark delamination at the transition zone to the base plate.
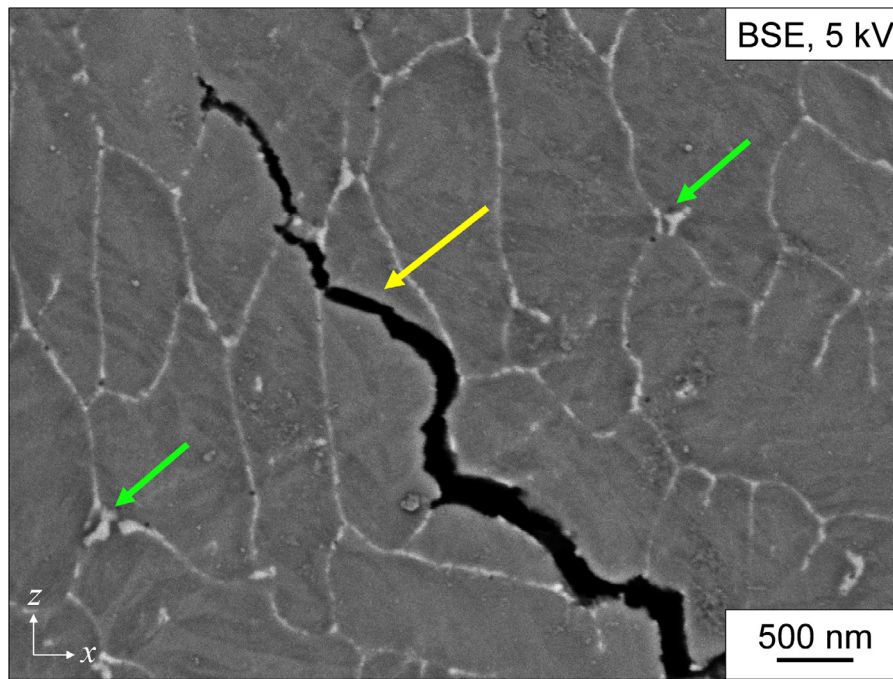
Fig. 5. BSE SEM micrograph of the crack propagation path. Except for the region marked by the yellow arrow, a clear correlation between brightly depicted network structures and crack propagation can be seen. The green arrows mark crossing points in the network structure.

hibit a more pronounced (inverted) C-shaped characteristics. Tensile strains were found in the topmost layers for both, martensite and austenite. However, maximal strain levels for both phases are lower than those of their counterparts determined in the center scan. The gray arrow in Fig. 4 (c, d) marks a difference in etching attack for the top layers in comparison to tempered layers in lower sample regions. Furthermore, Fig. 4 (d) documents a steep strain decrease from tensile into the compression regime for both phases directly beneath the topmost layers. This result correlates with the LOM images, as no cracking can be observed in the same area. The rest of the AM sample is subjected to tensile strains. The austenite strain profile reveals the same characteristic as the one determined for martensite but the strain level is slightly lower throughout the whole sample. In Fig. 4 (c), a longitudinal/transverse section of sample 100, that is rotated by 90° with respect to Fig. 4 (a), is shown. The blue arrow in Fig. 4 (a, c) indicates a delamination, which extends over the entire sample thickness and results in a relaxation of the measured martensite strain to zero. In addition, the occurrence of cracks starting from the sample edge is evident. Horizontal dashed lines correlate the observed strain drops to the positions of the particular horizontal cracks. It can be seen that tensile strains within martensite as well as austenite phases relax significantly to lower tensile strain levels at each crack position resulting in a zig-zagged strain profile, which was measured at the sample edge (Fig. 4 (d)).

For sample 50, strain profiles were determined at the same lateral positions - i.e., the center (Fig. 4 (e)) and the edge (Fig. 4 (g)) - like for sample 100. The following comparable results can be deduced. Firstly, the topmost layers exhibit tensile strains that are higher in martensite than in austenite and absolute strain levels are higher in the center of the sample than at its edge. Secondly, a comparable martensite strain profile characteristic, i.e., in this case a change from high tensile to compressive strains, can be seen in the edge scan where at the same time, the evaluation of $\varepsilon_{xx}^{hkl}(z) - \varepsilon_{zz}^{hkl}(z)$ in the center scan revealed the presence of tensile residual strains in the austenite. Thirdly, in the edge scan a compression strain regime is again obvious directly beneath the topmost lay-

ers that returns into the tensile regime with increasing distance to the topmost layer at the sample edges but again drops to zero at the interface to the base plate. The latter can be correlated to the longitudinal/transverse section in Fig. 4 (f) that depicts a continuous delamination at the interface to the base plate. This delamination is indicated by the blue arrow in Fig. 4 (f, g). However, a clear difference can be observed: there is no relation between crack occurrence and strain relaxations as sample 50 does not contain such apparent cracks like sample 100. A closer look only reveals the presence of a microcrack initiating from an internal pore (see red arrow in the inset of Fig. 4 (f)). Moreover, Fig. 4 (f) shows the variable melt pool depth induced by the pulsed wave emission. As the scan direction is rotated after each layer, the penetration of the melt pool to the previous layer and to the baseplate can vary locally. The pores are often found at the root of the keyholes.

3.2. Investigation of immediate crack proximity and crack surface morphology using SEM

To assess a possible correlation between the crack morphology and microstructural constituents in sample 500, a longitudinal/transverse sectional polish of the base plate interface delamination, as indicated by the white arrow in Fig. 2 (a), was examined in the SEM in BSE mode. Fig. 5 shows crack propagation running through the sample in a zig-zag way. Furthermore, a network of brightly depicted structures can be seen. It can be clearly deduced that, with exception of the area marked by the yellow arrow, the crack branches according to this network. The width of the bright network structures is below 100 nm. It appears that directional changes in crack propagation occur at crossing points of these dendritic structures (exemplarily marked by green arrows). The size of these almost spherically shaped constituents at such crossing points is in the range of ∼150 nm.

The direct investigation of the crack surface morphology has been carried out on the forced fracture surface at the remaining longitudinal/transverse section (Fig. 2(b)). Fig. 6 depicts SEM fractographs that were taken at an acceleration voltage of 3 kV in SE
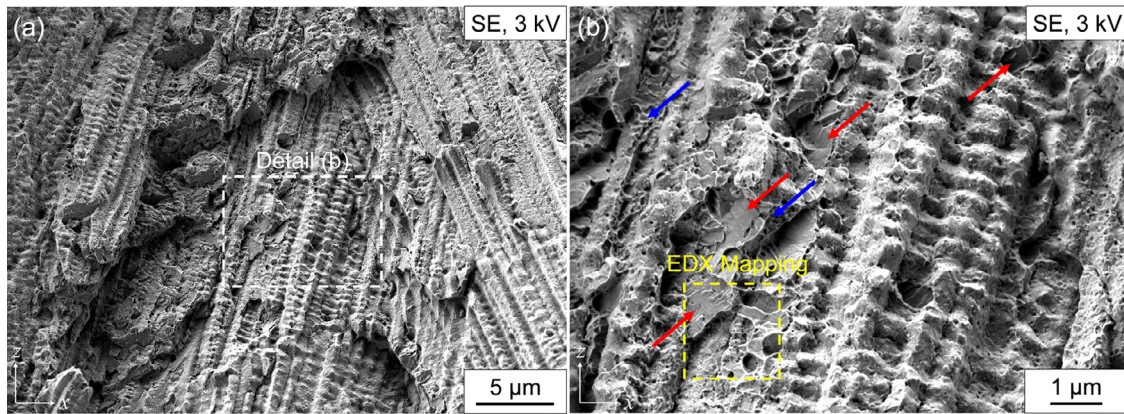
Fig. 6. SEM fractographs of the crack surface morphology at (a) low and (b) high magnification. Dendritic superstructures can be clearly seen. The red arrows mark cleavage fracture areas and the blue indicate dimpled fracture areas. The yellow dashed area marks the region of the EDX mapping depicted in Fig. 7.

mode. Dendritic superstructures are clearly visible in the fractograph in Fig. 6 (a). A detailed image of these structures is shown in Fig. 6 (b), which reveals extraordinarily fine features on the cracked surface. As already apparent in Fig. 5, a clear correlation between dendritic superstructures and crack propagation can be observed here too. Crack propagation obviously runs mainly along fracture surface structures that can neither be declared as cleavage nor as dimpled fracture areas. Cleavage fracture areas are marked by red and dimpled areas by blue arrows. Either one or both of these crack characteristics are assumed to be present at the yellow marked area in Fig. 5. However, the majority of the surface comprises of the abovementioned structures. In order to analyze possible differences in chemical composition to cleavage fracture areas, an EDX mapping has been performed. The investigated area is marked by the yellow dashed square in Fig. 6 (b).

3.3. Analysis of the crack surface chemical composition by EDX and APT

Fig. 7 depicts EDX concentration maps for Fe, C and the carbide-forming elements V, Mo and W. Fig. 7 (a) shows a SE fractograph of the mapped area that can be divided into three regions. Region A depicts cleavage fracture areas on the crack surface. Dimples can be assumed on the crack surface in region C. In contrast, region B shows the abovementioned structures that could not be clearly assigned as cleavage nor as dimple fracture areas. Certain areas of the concentration maps (i.e., upper right and lower left corner) are not accessible by the detector because of shielding effects of cavernous regions due to the roughness of the fracture surface. It can be qualitatively deduced from the elemental maps in Fig. 7 (b-f) that, in contrast to regions A and C, region B exhibits an enrichment in C, V, Mo and W. In addition, a significant depletion of Fe is evident in region B. However, typical elements that may be incorporated in hot or solidification cracking (i.e., S and P) could not be evaluated as no measurable signal was determined in the EDX spectra.

In addition to the EDX mapping, APT was used to verify the obtained qualitative results. APT enables determination of chemical composition of phases that are directly involved in crack formation on an atomic level. Fig. 8 (a) shows a 3D reconstruction of an exemplary APT tip taken directly from the Ag coated crack surface in sample *500* as described in section 2.3. Besides Fe and Ag ions, an isoconcentration surface with 15 at% C is shown. It can be seen that this isosurface is localized directly beneath the Ag coating. Therefore, a cylindrical region of interest (ROI, Ø15 nm) was used to analyze the chemical composition at this transition zone

representing the crack surface. As the cylinder was positioned almost perpendicular to the isosurface, the interface to the Ag coating represents a rather homogenous transition. The corresponding one-dimensional concentration profile (increment 0.2 nm) along the z-direction of the blue cylinder is shown in Fig. 8 (b). The width of the C-enriched zone amounts to approximately 15 nm. Additionally, high amounts of Mo, Cr and V were determined in this area.

To compare local chemical composition and size of the microstructural constituents, electrolytically prepared APT tips were taken from crack-free regions in tempered layers (sample *1000*). Fig. 8 (c) exemplarily shows a 3D reconstruction. C-rich constituents are again obvious and from their composition and the high C level it can be concluded that they represent carbides. In Fig. 8 (d), the corresponding concentration profile (increment 0.4 nm) along the blue cylindrical ROI (Ø15 nm) is shown. It is obvious that in the reconstruction the carbide, here confined by a 15 at% C isosurface, is larger than the sample volume and is therefore not completely displayed. Within the isosurface, a significant depletion in Fe and Co in comparison to the matrix composition is apparent. It has to be noted that the transition to the surrounding matrix is rather steep for all participating elements. The mean elemental compositions in the carbide were obtained from a z-range between 70 and 110 nm in Fig. 8 (d) and are (in at%): Fe=5.8±1.2, W=3.8±0.8, C=35.6±2.6, Co=0.1±0.1, Mo=11.6±1.7, Cr=11.0±1.5 and V=30.1±2.6.

3.4. TEM investigations of microstructural constituents

In order to determine the crystal structure of phases that are involved in cracking, a TEM lamella was prepared from the delamination zone at the base plate interface, see Fig. 9 (a).
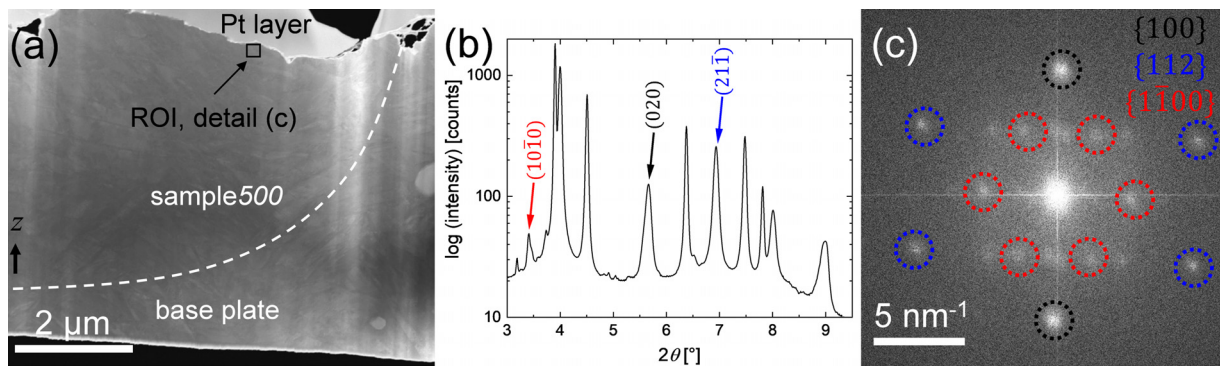
The white dashed line depicts the interface to the base plate. Fig. 9 (b) shows an exemplary HEXRD diffractogram (data acquired from sample *100*, center scan), which reveals martensite and austenite peaks, whereas the latter will not be further discussed in this work. Two martensite peaks with reciprocal lattice spacings of $d^{-1}_{(020)} = 6.942$ nm^{-1} and $d^{-1}_{(21\bar{1})} = 8.500$ nm^{-1} and one potential hexagonal M$_2$C carbide peak with $d^{-1}_{(10\bar{1}0)} = 4.179$ nm^{-1} are marked by the arrows. Fig. 9 (c) illustrates a fast Fourier transformed TEM micrograph of the ROI shown in Fig. 9 (a). Therein, cubic {100} (black) and {112} (blue) and hexagonal {1$\bar{1}$00} (red) diffraction spots can be seen. The respective reciprocal lattice spacings are: $d^{-1}_{\{100\}} = 6.974 \pm 0.022$ nm^{-1}, $d^{-1}_{\{112\}} = 8.423 \pm 0.084$ nm^{-1} and $d^{-1}_{\{1\bar{1}00\}} = 4.147 \pm 0.057$ nm^{-1}.
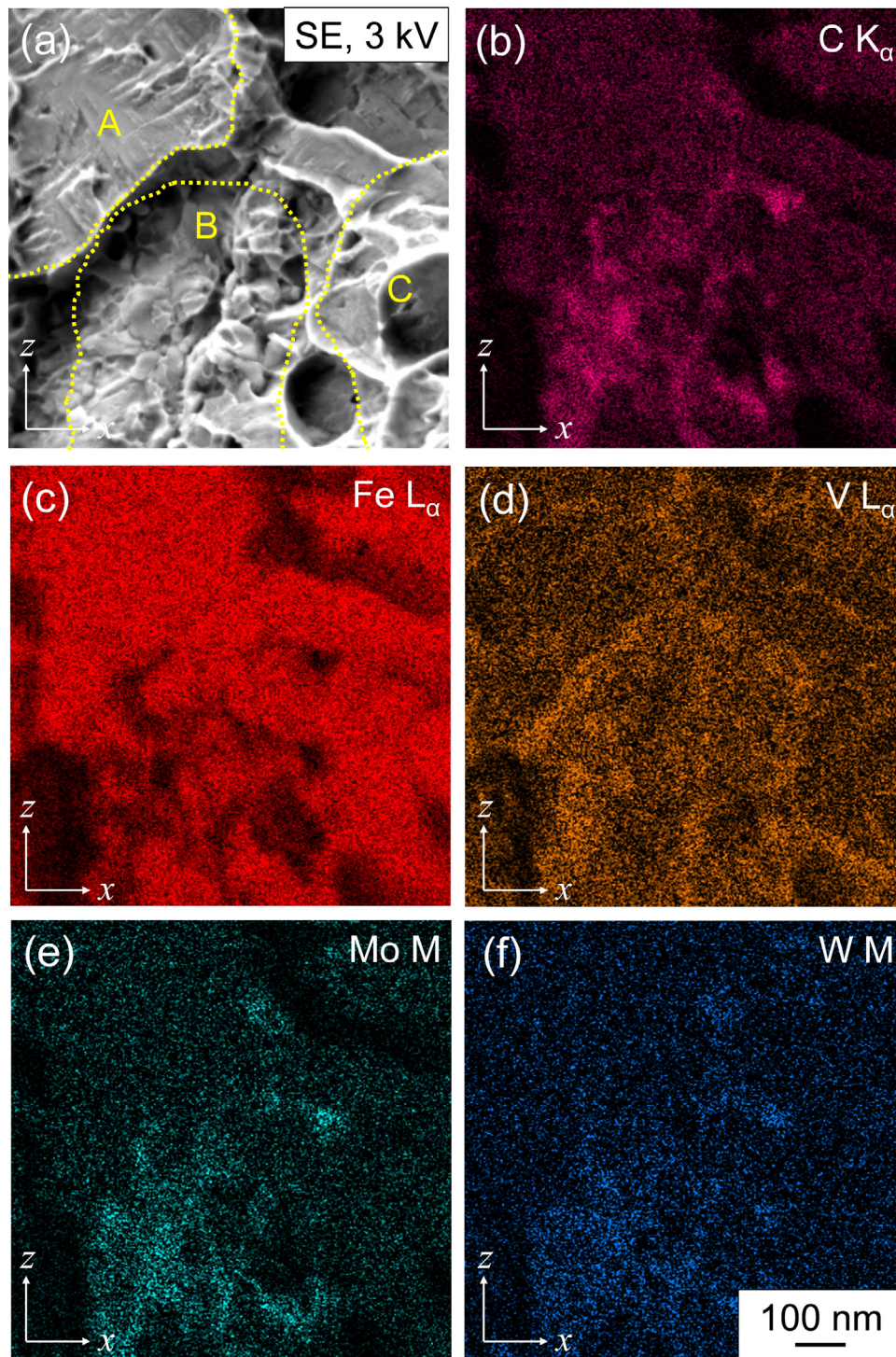
Fig. 7. EDX concentration maps on the crack surface. Three regions are indicated by the yellow dashed lines in (a). In contrast to A and C, region B depicts a significant enrichment in C, V, Mo and W.
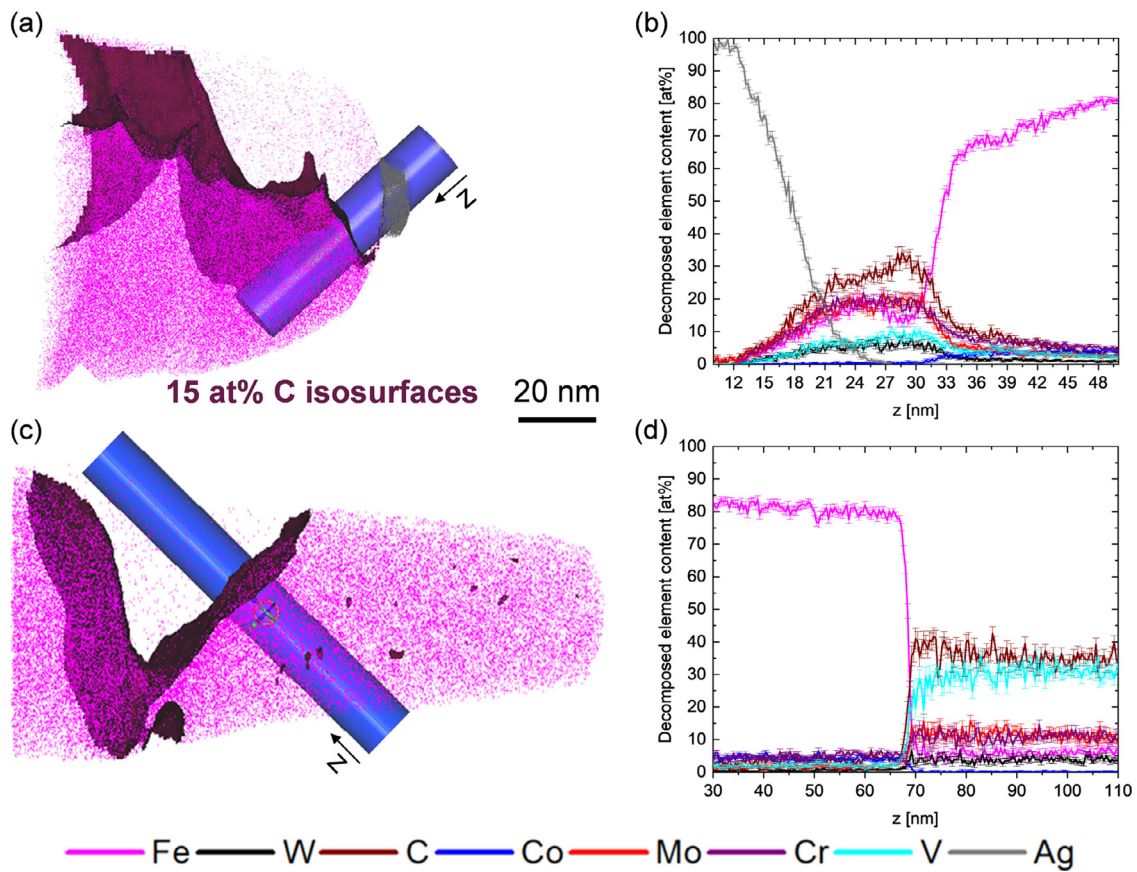
Fig. 8. 3D reconstructions of exemplary APT tips and corresponding concentration profiles along the z direction of the blue cylinders: (a, b) APT analysis at the crack surface (sample500); (c, d) APT analysis of a crack-free area in tempered layers (sample1000).

Fig. 9. (a) Overview of the TEM lamella taken from the base plate interface (sample500), which is marked by the white dashed line. (b) HEXRD diffractogram depicting phases for TEM evaluation. (c) Fast Fourier transformed TEM micrograph depicting martensite and M_2C carbide diffraction spots in the immediate vicinity of a crack.

It is reasonable to assume that the six diffraction spots, which are marked by the red circles, can be assigned to the abovementioned hexagonal M_2C carbide structure.

4. Discussion

The objective of the present study was to analyze the cracking mechanism in a LPBF carbon-containing cold-work tool steel. As cracking during AM is basically a stress-driven phenomenon, strain in dependence of different sample heights was determined using synchrotron radiation and correlated to the position and the appearance of cracks by means of metallographic longitudinal/transverse sectional polishes using LOM. To characterize the manner of the crack propagation, the immediate crack vicinity and

crack surfaces were characterized using SEM. In order to determine the chemistry of phases that are directly involved in crack formation and propagation, an EDX mapping and APT measurements were performed on tips taken directly from the crack surface. The obtained results will be merged in this section and discussed to propose a theory for the predominant cracking mechanism in the investigated tool steel.

The measured strain profiles showed clear differences between the scans taken in the center and the edges of the samples. A C-shaped martensite strain profile was determined for the center in the case of sample100, see Fig. 4 (b). Tensile strains in austenite were characterized in the center scans of both samples. This is atypical according to stress measurements performed by Yan *et al.* [56], who have been reporting the development of compres-

sive stresses in the austenite in a LPBF hot-work tool steel due to martensite transformations as the latter comes along with a volume expansion [30]. As this phenomenon does not directly influence the cracking behavior observed at the sample edges and would also exceed this work's scope, future research on potential austenite stabilization mechanisms in carbon-containing LPBF tool steels will be conducted.

Strain profile measurements were also conducted at the edges of both samples (Fig. 4 (d) and (g)). It is obvious, that the top layers are subjected to tensile strains. The temperature gradient mechanism (TGM) model proposed by Mercelis *et al.* [57] can be used to explain these differences between the top and the tempered layers in the edge scan. During LPBF, a steep temperature gradient evolves due to very localized laser energy input and rather slow heat conduction. As the yield strength of a material is reduced at higher temperatures and the expansion of the top layers is restricted by the underlying material (i.e., the tempered layers or the base plate), the top region will be plastically compressed if the materials yield strength is exceeded. Upon cooling, this region shrinks, which leads to the induction of tensile stresses in the plastically deformed areas and compressive stresses in underlying areas. This effect can be further intensified if the material is molten during the process, which is the case during LPBF but not for example in selectively laser sintered materials. The lower strain level of the austenite in comparison to the martensite in the edge scans can be interpreted by the formation of additional martensite during cooling. Thus, austenite is further strained into the compression regime by the volume expansion caused by the martensite formation. Besides the TGM model, the differences in the strain magnitude in the top layers can possibly be attributed to the variations of the longitudinal/transverse sectional microstructure. The latter are indicated by the gray arrows in Fig. 4 (c, d) and (f, g) and are mainly caused by the lack of in-situ tempering processes during LPBF in comparison to the underlying layers. All strain profiles exhibited large areas with tensile strains but in contrast to the center scan, strains in the topmost layers are tensile at the edge as the state of stresses is 90° rotated with respect to the stress state at the center. The rotated state of stresses at the edge goes hand in hand with the orientation of cracking observed in Fig. 4 (c). To clarify the phenomenon of occurring compressive and tensile strains in the topmost layers, residual stress development considerations proposed by Dilthey *et al.* [58] during hardening of a cylinder are taken into account. A significant difference in cooling rates between the edge and the core of this cylinder is apparent during water quenching. The higher cooling rate at the edge yields an increased shrinkage at the beginning of the cooling cycle. Due to mutual strain constraints, the edge is subjected to tensile stresses while the core is under compressive loads. As the core is exposed to higher temperatures due to lower cooling rates, this region is plastically compressed because of the temperature dependent reduction of the yield strength. At the end of the cooling cycle, the temperatures of core and edge are equalized resulting in compressive stresses at the edge and tensile stresses in the core. This can again be attributed to the mutual strain constraint. In the present case, this phenomenon has to be considered in the opposite direction as the sample edges are surrounded on one side by the powder bed, which has a significantly lower thermal conductivity than already built solid bulk structures [59]. Therefore, the presence of tensile stresses causing crack formation can be explained by lower cooling rates at the sample edges.

The correlation between strain evolution at the sample edges and LOM longitudinal/transverse sections in Fig. 4 (c, d) and (f, g) yielded two major findings. Firstly, the extinction of martensite strains to zero at distances to the top layer of ∼2.75 mm and ∼1.45 mm, respectively, representing the interfaces between AM material and base plate in the investigated samples. In advance to crack formation, these transition zones have been in the tensile strain regime, as can be seen by means of the martensite strain profiles that were determined in crack-free areas of the sample center, see Fig. 4 (b) and (e). The sharp junction (transition angle of 90°) between base plate and AM material apparently acts as a zone with an increased notch sensitivity. Thus, a strain concentration arises at the sample edge between base plate and AM material, which is completely relieved by the formation of an end-to-end delamination.

Secondly, the LOM longitudinal/transverse section in Fig. 4 (f) clearly showed that, apart from the delamination at the transition zone between AM material and base plate and the local microcrack starting from a geometrically notched lack-of-fusion pore (inset of Fig. 4 (f)), the smaller sample*50* contains no cracks. In contrast, the occurrence of cracks in the middle part of the larger *sample100*, which is depicted in Fig. 4 (c), and the resulting stress relaxations could be clearly correlated to each other, as shown by the black dashed arrows in Fig. 4 (c, d). At the positions where cracks are present, the tensile strains are relieved. This occurs through the formation of cracks and can be clearly deduced as local tensile strain decreases in Fig. 4 (d) resulting in the measured zig-zag strain profile. The presence of these cracks can also serve to elucidate the generally higher tensile strain level determined in the smaller sample. As the measured profiles depict the strain conditions in the as-built state after the process is completed, it can be concluded that during the process the strain level must have been higher at the edges of sample*100* to cause the observed crack formation. It can therefore be assumed that a minimum part height is mandatory to incorporate sufficiently high strain accumulations during the layer-by-layer LPBF process to form cracks in the investigated samples. Cracking is caused, if the materials local rupture resistance is exceeded. For the present study, this height evidently lies beneath 1.5 mm (sample*50*) and 3 mm (sample*100*). To assess the point when in the process this stress-related cracking phenomenon takes place, in-situ process monitoring would be necessary.

When the melt pool size is taken into account, which is in the range of several tens of microns according to the chosen process parameters (see section 2.1), the obtained results also allow the conclusion that crack formation has occurred in the solid state as cracks range over larger zones.

SEM micro- and fractographs in Fig. 5 and Fig. 6, respectively, revealed that crack propagation branches in relation to the dendritic superstructures. This continuous network represents the solidification structure of the material as a result of the LPBF process. The extremely fine morphology of these dendritic structures can be attributed to extraordinarily high solidification rates. According to finite element analysis simulations performed by Chen *et al.* [60], possible cooling rates during LPBF are in the order of 10^7 K/s.

At positions where these carbides converge (marked by green arrows in Fig. 5 (b)), it comes to a change in crack propagation direction. Although cracks propagate mainly along these carbide network, the yellow arrow in Fig. 5 (b) indicates that cracks may also diffuse through the matrix at some positions. The detailed view of the fractograph in Fig. 6 (b) reassured that crack propagation mainly runs through these dendritic network structures, which are formed during solidification. However, certain fracture areas were observed, that exhibit cleavage failure and dimpled fracture elements. These areas represent regions at which crack propagation differs from its predominant path along the dendrite network. Based on previous investigations, the microstructure of the investigated steel comprises of martensite, austenite and carbides [37]. Basically, brittle martensite exhibits transcrystalline cleavage fracture planes due to its high barrier for dislocation movement [61]. Therefore, the transcrystalline fracture surfaces shown

in Fig. 6 (b) can possibly be associated to martensite failure. In contrast, austenite typically shows pull-out fracture features that can possibly be assigned to the observed dimpled fracture areas. These dimples could, however, also have been formed as a result of austenite seams that surround almost spherically shaped carbides and were pulled out due to thermal stresses.

A first indication of the chemical composition of the carbide network structures, along which cracks propagate, is provided by Fig. 5 as heavy elements appear more brightly in the BSE detection mode of a SEM [62]. Hence, it can be concluded that these dendritic network structures can be identified as carbides, which are enriched in Mo and W. In order to analyze the chemical composition of such microstructural features with dimensions below 100 nm, methods with high spatial resolution are necessary. Furthermore, the interaction volume of the electron beam during EDX must be in the range of the structures of interest. EDX investigations with conventional large area silicon drift detectors do not facilitate accurate analysis as the electron beamś interaction volume in pure Fe at 20 kV is in the micrometer range [62]. According to Monte Carlo simulations [63,64], the interaction volume depth of Fe L_α X-rays at the chosen acceleration voltage of 3 kV within pure Fe is approximately 50 nm. Hence, this acceleration voltage has been used. With this EDX mapping, chemical information could be obtained from, compared to APT dimensions, a relatively large area of the crack surface.

The determined EDX map in Fig. 7 (a) was divided into three regions. Region A depicted a typical martensite cleavage fracture plain and region C showed dimpled fracture structures that could be formed due to failure of austenite or ductile pull-out of austenite seams that surround spherical carbides. In terms of the chemical composition, region B showed significant enrichment in C, V, Mo and W compared to regions A and C. As these elements are necessary for carbide formation, it can be stated that crack propagation can be directly correlated to the presence of carbides in region B. The measured depletion of Fe additionally supports this statement [65]. Concerning the sub 100 nm fracture surface structures in region B, no clear statement can be made about whether failure occurs along carbide boundary regions or directly through the carbides. From the EDX mappings, no difference in chemical composition could be observed between region A and C. This indicates that austenite is not chemically stabilized as no qualitative C-enrichment compared to martensite was detected.

APT investigations were performed on tips that were directly taken from the crack surface to allow chemical analysis on an atomic level. By applying the tip preparation procedure described in section 2.3, it could be guaranteed that the crack surface is within the analysis volume. Impurity elements (i.e., S and P) are often responsible for the occurrence of low melting eutectic phases that often occur in interdendritic areas or at grain boundaries. In combination with process-related stresses, the impurity elements basically cause hot respectively solidification cracking during welding processes [66–68]. Via APT evaluation, no such impurity element segregations could be determined within the region directly beneath the Ag layer (i.e., on the crack surface). Combined with the abovedescribed correlations between crack occurrence and measured strain profiles, the formation of classical hot cracks (i.e., hot-tearing or solidification cracking) is therefore excluded. Instead, the results presented in Fig. 8 (a, b) clearly depicted the presence of C-rich constituents on the crack surface. At z>27 nm, where the incorporation of Ag is reduced to zero, a carbon content above 30 at% which clearly indicates the presence of carbides, has been determined. Carbide formation in dependence of the chosen laser power in a selectively laser sintered M2 HSS (~HS 6-5-2 with approx. 1wt% C) has already been observed by Niu et al. [69]. By means of XRD and EDX measurements, they found increasing contents of Fe-, Mo and W-rich M_6C and Fe- and V-rich M_4C_3 carbides

at cell boundaries with rising energy input, i.e., higher laser power. In addition, continuous brittle grain boundary carbide networks in the as-solidified state were also found by Wright et al. [70] and Liu et al. [71] in M2 HSS. This is in accordance with the present work, in which continuous network structures that formed during solidification have also been determined.

Regarding microstructural development during LPBF, Sander et al. [72] published a model for a FeCr4Mo1V1W8C1 (wt%) alloy based on non-equilibrium segregation of alloying elements. They performed electron backscatter diffraction and concluded on the presence of retained austenite directly next to carbide dendrites. In addition, their XRD experiments revealed a lower content of C and carbide-forming elements in the martensite than in the austenite next to the carbides. They concluded that this element reduction enables the transformation of former austenite to martensite during cooling in the center regions of the dendrites that formed during solidification. A similar theory for the formation of dendritic structures as a result of rapid solidification was published by Wu et al. [73] for AISI H13 hot-work tool steel. They also reported elemental segregations resulting in austenite stabilization and V-rich carbides at grain respectively dendrite boundaries.

In the present study, the concentration profile in Fig. 8 (d) shows a steep decrease in C and other elements (i.e., W, Mo, V and Cr) at z=70 nm, which decrease the martensite start temperature of the investigated steel [74]. By taking the abovementioned elemental segregation mechanisms [72,73] during solidification and subsequent cooling into account, it can be assumed that these constituents comprise of an eutectic mixture of carbides and austenite. Therefore, no difference in chemical composition between martensite and austenite and consequently no chemical stabilization of the austenite can be deduced from the conducted APT experiments. As the investigated steel contains a significant amount of austenite in the as-built state according to HEXRD phase analysis, other austenite stabilization mechanisms must prevail, which are furthermore supposed to cause the unusual presence of tensile residual stresses in austenite (center scan) and are the subject of future research activities.

Due to their dendritic morphology (cf. Fig. 5), the carbidic constituents on the crack surface obviously formed during solidification. A comparison of their widths at the crack surface (<15 nm) with the dimensions of eutectic carbides in crack-free areas of tempered layers (>20 nm) indicates that crack propagation runs through these constituents in a transgranular manner. However, APT reconstruction parameters strongly influence the determination of dimensions (cf. section 2.3). Therefore, the mean carbide widths were determined for k_f=2, 5, 8 and amount to 14, 17, and 19 nm for the tip from the crack surface (Fig. 8 (a)) and 20, 65 and 170 nm for the electrolytic tip (Fig. 8 b) from a crack-free area in a tempered layer, respectively. Although these determined carbide widths should only be treated as indicative instead of absolute values, it can be estimated that the smallest possible carbide width in the microstructure (20 nm) is still larger than the largest possible width determined underneath the crack surface (19 nm).

In terms of chemical composition determined on the crack surface as well as in crack-free areas, APT indicates (C~30…35 at%, cf. Fig. 8 (b, d)) that these eutectics are mixed carbides of the type M_2C, where M = V, Cr, Mo, Fe and W. Besides high amounts of martensite due to strong diffraction spots, TEM diffraction experiments in Fig. 9 proved the presence of carbides that can be assigned to M_2C type as a comparison of the reference reciprocal lattice distances taken from HEXRD data and the determined values for the M_2C carbides are in good accordance by taking the measured standard deviation into account. This result contradicts an investigation by Liu et al. [75] on LPBF M2 HSS. Besides the beneficial impact on processability by mitigating cracking through base plate preheating, they reported a lack of expected M_2C car-

bide peaks in XRD diffractograms in the as-built state. However, this may be explained by the fact that the investigated cold-work tool steel in the present study significantly differs from M2 HSS.

Based on the obtained and abovediscussed results, it can be concluded that stress accumulations are necessary to initiate crack formation from the sample edges. These accumulations either evolve as a result of thermal stresses by applying at least 50 layers in the LPBF process or because of geometrically notched specimen positions (i.e., base plate interface or internal pores) or most probably due to a combination of both for the investigated sample geometry. After initiation, these cracks apparently branch according to a carbide network, which formed during solidification. This network comprises of brittle eutectic carbides and definitely fails through solid-state cracking. A comparison of carbide widths determined directly underneath the crack surface and carbides taken in crack-free areas indicates that crack propagation runs through the carbides in a transcrystalline manner.

In order to avoid failure along the dendritic solidification structure, two general approaches can be chosen. Firstly, the strain level could be reduced by lowering the process-related thermal gradient. This could result in strains that no longer exceed the materials̍ rupture strain and can be achieved by applying a base plate preheating unit. However, the use of conventional base plate heating methods may be insufficient due to the low temperature levels employed and the heat source being fixed to the bottom of the plate. Especially for small parts, the latter seems like a promising approach. However, the results showed that severe cracking occurs during the fabrication of bulky geometries and around the geometrical transition zones such as pointy edges. For those, further heating devices may be established (i.e., local heating of the powder bed by infrared lamps or defocusing as in electron beam melting). In order to account for the delamination at the interface between base plate and AM material, support structures could be helpful as they can be designed in a way that a smoother transition is guaranteed. Design of the part and the support structures can be further studied coupled to the numerical simulations to reduce the risk of cracking, while reducing the design freedom of LPBF to a certain extent. Secondly, cracking could be overcome by adapting the chemical composition of the processed alloy. This could be accomplished for example by substituting carbide-forming elements, which preferably form the determined eutectic carbides of M_2C type. A potential shift away from eutectic to primary carbides such as MC or M_6C carbides could be a promising approach. These carbide types are basically decomposition products of metastable M_2C carbides [76,77] that decay at high temperatures during heat input from subsequent fabrication stages after conventional casting. Therefore, a third approach would be to induce such a decomposition treatment during LPBF by for example double scanning with appropriate adaption of laser process parameters.

5. Conclusions

The aim of the present work was to assess the predominant cracking mechanism in a LPBF cold-work tool steel. The following conclusions can be drawn by merging the conducted experiments:

1. Residual strain profiles were determined at different sample positions and for different sample heights. Longitudinal/transverse sectional LOM investigations showed a clear relation between stress relieving processes and the positions at which cracking occurs. Therefore, stress accumulations, which form as a result of thermal stresses during the layer-by-layer LPBF process, are made responsible for solid-state cracking. For the analyzed part geometry, i.e., rectangular cross-section, a minimum part height of 50 layers is necessary to cause cracking from the sample edges.

2. Geometrically notched positions, i.e., the sample edge, the interface between base plate and AM material or internal pores, cause stress concentrations and are hence sites for crack initiation.

3. Fractography and SEM investigations of the immediate crack proximity (longitudinal/transverse sectional polishes) revealed an apparent correlation between crack propagation and dendritic superstructures, which obviously formed during solidification.

4. To qualitatively determine which chemical elements are involved in crack formation, an EDX mapping was conducted on the crack surface. The results indicated the presence of C-enriched phases on the majority of the crack surface. The presence of eutectic carbides of type M_2C was finally revealed by APT analysis and TEM investigations.

5. In summary, a clear relation between a network comprising of eutectic carbides, which was formed during solidification but definitely fails through stress accumulations in the solid state is evident. This has been assigned as predominant cracking mechanism for the investigated cold-work tool steel fabricated with LPBF. Furthermore, a comparison of carbide widths determined at the crack surface and from crack-free areas indicates that crack propagation preferably runs through these carbides in a transcrystalline way.

Declaration of Competing Interest

The authors declare that they have no known competing financial interests or personal relationships that could have appeared to influence the work reported in this paper.

Acknowledgments

References

[1] I. Gibson, D. Rosen, B. Stucker, Additive Manufacturing Technologies, Springer, New York, 2015.

[2] D. Herzog, V. Seyda, E. Wycisk, C. Emmelmann, Additive manufacturing of metals, Acta Mater. 117 (2016) 371–392.

[3] B.P. Conner, G.P. Manogharan, A.N. Martof, L.M. Rodomsky, C.M. Rodomsky, D.C. Jordan, J.W. Limperos, Making sense of 3-D printing: creating a map of additive manufacturing products and services, Addit. Manuf. 1 (2014) 64–76-4.

[4] A. Gebhardt, Understanding Additive manufacturing: Rapid prototyping, Rapid tooling, Rapid Manufacturing, Hanser, Munich, 2012.

[5] J. Sander, J. Hufenbach, L. Giebeler, H. Wendrock, U. Kühn, J. Eckert, Microstructure and properties of FeCrMoVC tool steel produced by selective laser melting, Mater. Des. 89 (2016) 335–341.

[6] M. Mazur, M. Leary, M. McMillan, J. Elambasseril, M. Brandt, SLM additive manufacture of H13 tool steel with conformal cooling and structural lattices, Rapid Prototyp. J 22 (2016) 504–518.

[7] S. Kou, A criterion for cracking during solidification, Acta Mater. 88 (2015) 366–374.

[8] J. Campbell, Castings, Butterworth Heinemann, Oxford, 2003.

[9] S. Kou, Welding Metallurgy, John Wiley and Sons, Hoboken, 2013.

[10] M. Rappaz, J.M. Drezet, M. Gremaud, A new hot-tearing criterion, Metall. Mater. Trans. A 30 (1999) 449–455.

[11] Z. Sun, X.P. Tan, M. Descoins, D. Mangelinck, S.B. Tor, C.S. Lim, Revealing hot tearing mechanism for an additively manufactured high-entropy alloy via selective laser melting, Scr. Mater. 168 (2019) 129–133.

[12] Z. Sun, X. Tan, C. Wang, M. Descoins, D. Mangelinck, S.B. Tor, E.A. Jägle, et al., Reducing hot tearing by grain boundary segregation engineering in additive manufacturing: example of an AlxCoCrFeNi high-entropy alloy, Acta Mater. 204 (2021) 116505.

[13] C. Zhang, K. Feng, H. Kokawa, B. Han, Z. Li, Cracking mechanism and mechanical properties of selective laser melted CoCrFeMnNi high entropy alloy using different scanning strategies, Mater. Sci. Eng. A 789 (2020) 139672.

[14] D. Tomus, P.A. Rometsch, M. Heilmaier, X. Wu, Effect of minor alloying elements on crack-formation characteristics of Hastelloy-X manufactured by selective laser melting, Addit. Manuf. 16 (2017) 65–72.

[15] M. Cloots, P.J. Uggowitzer, K. Wegener, Investigations on the microstructure and crack formation of IN738LC samples processed by selective laser melting using Gaussian and doughnut profiles, Mater. Des. 89 (2016) 770–784.

[16] Z. Hu, H. Zhu, H. Zhang, X. Zeng, Experimental investigation on selective laser melting of 17-4PH stainless steel, Opt. Laser Technol. 87 (2017) 17–25.

[17] S. Sarkar, S. Mukherjee, C.S. Kumar, A. Kumar Nath, Effects of heat treatment on microstructure, mechanical and corrosion properties of 15-5 PH stainless steel parts built by selective laser melting process, J. Manuf. Process. 50 (2020) 279–294.

[18] R. Tewari, S. Mazumder, I.S. Batra, G.K. Dey, S. Banerjee, Precipitation in 18 wt% Ni maraging steel of grade 350, Acta Mater. 48 (2000) 1187–1200.

[19] U.K. Viswanathan, G.K. Dey, M.K. Asundi, Precipitation hardening in 350 grade maraging steel, Metall. Trans. A 24 (1993) 2429–2442.

[20] C. Tan, K. Zhou, M. Kuang, W. Ma, T. Kuang, Microstructural characterization and properties of selective laser melted maraging steel with different build directions, Sci. Technol. Adv. Mater. 19 (2018) 746–758.

[21] A. Hadadzadeh, A. Shahriari, B.S. Amirkhiz, J. Li, M. Mohammadi, Additive manufacturing of an Fe–Cr–Ni–Al maraging stainless steel: microstructure evolution, heat treatment, and strengthening mechanisms, Mater. Sci. Eng. A 787 (2020) 139470.

[22] , Microstructure and mechanical properties of maraging steel 300 after selective laser melting, in: E. Yasa, K. Kempen, J.P. Kruth (Eds.), Proceedings of the International Solid Freeform Fabrication Symposium, Texas, Austin, 2010 August 9-11.

[23] F. Deirmina, N. Peghini, B. AlMangour, D. Grzesiak, M. Pellizzari, Heat treatment and properties of a hot work tool steel fabricated by additive manufacturing, Mater. Sci. Eng. A 753 (2019) 109–121.

[24] R. Li, Y. Shi, Z. Wang, L. Wang, J. Liu, W. Jiang, Densification behavior of gas and water atomized 316L stainless steel powder during selective laser melting, Appl. Surf. Sci. 256 (2010) 4350–4356.

[25] M. Rombouts, J.P. Kruth, L. Froyen, P. Mercelis, Fundamentals of selective laser melting of alloyed steel powders, CIRP Ann. 55 (2006) 187–192.

[26] K. Geenen, A. Röttger, F. Feld, W. Theisen, Microstructure, mechanical, and tribological properties of M3:2 high-speed steel processed by selective laser melting, hot-isostatic pressing, and casting, Addit. Manuf. 28 (2019) 585–599.

[27] J. Boes, A. Röttger, C. Mücke, C. Escher, W. Theisen, Microstructure and mechanical properties of X65MoCrWV3-2 cold-work tool steel produced by selective laser melting, Addit. Manuf. 23 (2018) 170–180.

[28] J. Krell, A. Röttger, K. Geenen, W. Theisen, General investigations on processing tool steel X40CrMoV5-1 with selective laser melting, J. Mater. Process. Technol. 255 (2018) 679–688.

[29] L. Caprio, A.G. Demir, G. Chiari, B. Previtali, Defect-free laser powder bed fusion of Ti–48Al–2Cr–2Nb with a high temperature inductive preheating system, J. Phys. Photonics 2 (2020) 24001.

[30] G. Gottstein, Physikalische Grundlagen der Materialkunde, Springer-Verlag, Berlin, Heidelberg, Germany, 2007.

[31] R. Mertens, B. Vrancken, N. Holmstock, Y. Kinds, J.P. Kruth, J. van Humbeeck, Influence of powder bed preheating on microstructure and mechanical properties of H13 Tool steel SLM parts, Phys. Proced. 83 (2016) 882–890.

[32] H. Fayazfar, M. Salarian, A. Rogalsky, D. Sarker, P. Russo, V. Paserin, E. Toyserkani, A critical review of powder-based additive manufacturing of ferrous alloys: process parameters, microstructure and mechanical properties, Mater. Des. 144 (2018) 98–128.

[33] J. Saewe, C. Gayer, A. Vogelpoth, J.H. Schleifenbaum, Feasability Investigation for laser powder bed fusion of high-speed steel AISI M50 with base preheating system, Berg- Huettenmaenn. Monatsh. 164 (2019) 101–107.

[34] F. Feuerhahn, A. Schulz, T. Seefeld, F. Vollertsen, Microstructure and properties of selective laser melted high hardness tool steel, Phys. Proced. 41 (2013) 843–848.

[35] J. Jin, R. Gao, H. Peng, H. Guo, S. Gong, B. Chen, Rapid solidification microstructure and carbide precipitation behavior in electron beam melted high-speed steel, Metall. Mater. Trans. A 51 (2020) 2411–2429.

[36] J.P. Kruth, S. Kumar, J. van Vaerenbergh, Study of laser-sinterability of ferro-based powders, Rapid Prototyp. J. 11 (2005) 287–292.

[37] J. Platl, H. Leitner, C. Turk, A.G. Demir, B. Previtali, R. Schnitzer, Defects in a laser powder bed fused tool steel, Adv. Eng. Mater. 11 (2020) 2000833.

[38] N. Schell, A. King, F. Beckmann, H.U. Ruhnau, R. Kirchhof, R. Kiehn, M. Müller, et al., The high energy materials science beamline (HEMS) at PETRA III, in: Proceedings of the AIP Conference Proceedings, 2010, pp. 391–394. 2010.

[39] J. Kieffer, D. Karkoulis, PyFAI, a versatile library for azimuthal regrouping, J. Phys. Conf. Ser. 425 (2013) 202012.

[40] I.C. Noyan, J.B. Cohen, Residual Stress: Measurement by Diffraction and Interpretation, Springer, 2013.

[41] S.A. Kim, W.L. Johnson, Elastic constants and internal friction of martensitic steel, ferritic-pearlitic steel, and α-iron, Mater. Sci. Eng. A 452 (2007) 633–639.

[42] E. Kröner, Berechnung der elastischen konstanten des vielkristalls aus den konstanten des einkristalls, Z. Phys. 151 (1958) 504–518.

[43] J. Keckes, M. Bartosik, R. Daniel, C. Mitterer, G. Maier, W. Ecker, J. Vila-Comamala, et al., X-ray nanodiffraction reveals strain and microstructure evolution in nanocrystalline thin films, Scr. Mater. 67 (2012) 748–751.

[44] M. Stefenelli, J. Todt, A. Riedl, W. Ecker, T. Müller, R. Daniel, M. Burghammer, et al., X-ray analysis of residual stress gradients in TiN coatings by a Laplace space approach and cross-sectional nanodiffraction: a critical comparison, J. Appl. Crystallogr. 46 (2013) 1378–1385.

[45] S.C. Bodner, L.T.G. van de Vorst, J. Zalesak, J. Todt, J.F. Keckes, V. Maier-Kiener, B. Sartory, et al., Inconel-steel multilayers by liquid dispersed metal powder bed fusion: microstructure, residual stress and property gradients, Addit. Manuf. 32 (2020) 101027.

[46] S.C. Bodner, M. Meindlhumer, T. Ziegelwanger, H. Winklmayr, T. Hatzenbichler, C. Schindelbacher, B. Sartory, et al., Correlative cross-sectional characterization of nitrided, carburized and shot-peened steels: synchrotron micro-X-ray diffraction analysis of stress, microstructure and phase gradients, J. Mater. Res. Technol. 11 (2021) 1396–1410.

[47] Oxford Instruments Homepage. https://nano.oxinst.com/ultim-extreme, accessed in May 2021.

[48] T.T. Tsong, Field ion image formation, Surf. Sci. 70 (1978) 211–233.

[49] S. Monschein, R. Schnitzer, R. Fluch, C. Turk, C. Hofer, Atom probe tomography of the oxide layer of an austenitic stainless CrMnN-steel, Pract. Metallogr. 58 (2021) 264–281.

[50] B. Gault, M.P. Moody, J.M. Cairney, S.P. Ringer, Atom Probe Microscopy, Springer New York, New York, NY, 2012.

[51] B. Gault, A. La Fontaine, M.P. Moody, S.P. Ringer, E.A. Marquis, Impact of laser pulsing on the reconstruction in an atom probe tomography, Ultramicroscopy 110 (2010) 1215–1222.

[52] T. Sakurai, E.W. Müller, Field calibration using the energy distribution of field ionization, Phys. Rev. Lett. 30 (1973) 532.

[53] T. Sakurai, E.W. Müller, Field calibration using the energy distribution of a free-space field ionization, J. Appl. Phys. 48 (1977) 2618–2625.

[54] F. Vurpillot, B. Gault, B.P. Geiser, D.J. Larson, Reconstructing atom probe data: a review, Ultramicroscopy 132 (2013) 19–30.

[55] D.J. Larson, T.J. Prosa, R.M. Ulfig, B.P. Geiser, T.F. Kelly, Local Electrode Atom Probe Tomography, Springer New York, New York, NY, 2013.

[56] J.J. Yan, D.L. Zheng, H.X. Li, X. Jia, J.F. Sun, Y.L. Li, M. Qian, et al., Selective laser melting of H13: microstructure and residual stress, J. Mater. Sci. 52 (2017) 12476–12485.

[57] P. Mercelis, J.P. Kruth, Residual stresses in selective laser sintering and selective laser melting, Rapid Prototyp. J. 12 (2006) 254–265.

[58] U. Dilthey, A. Brandenburg, Schweißtechnische Fertigungsverfahren: Gestaltung und Festigkeit von Schweißkonstruktionen, 2nd ed., Springer, Berlin, Heidelberg, 2002.

[59] L.C. Wei, L.E. Ehrlich, M.J. Powell-Palm, C. Montgomery, J. Beuth, J.A. Malen, Thermal conductivity of metal powders for powder bed additive manufacturing, Addit. Manuf. 21 (2018) 201–208.

[60] H. Chen, D. Gu, D. Dai, C. Ma, M. Xia, Microstructure and composition homogeneity, tensile property, and underlying thermal physical mechanism of selective laser melting tool steel parts, J. Mater. Sci. Eng. A 682 (2017) 279–289.

[61] E. Dudrová, M. Kabátová, Fractography of sintered iron and steels, Powder Metall. Prog. 8 (2008) 59–75.

[62] J.I. Goldstein, D.E. Newbury, J.R. Michael, N.W.M. Ritchie, J.H.J. Scott, D.C. Joy, Scanning Electron Microscopy and X-ray Microanalysis, Springer, New York, 2017.

[63] Oxford Instruments Nanoanalysis Homepage. https://nano.oxinst.com/library/blog/extreme-tips-and-tricks, accessed in May 2021.

[64] S. Burgess, J. Sagar, J. Holland, X. Li, F. Bauer, Ultra-low kV EDS – a new approach to improved spatial resolution, surface sensitivity, and light element compositional imaging and analysis in the SEM, Microsc. Today 25 (2017) 20–29.

[65] G.A. Roberts, R. Kennedy, G. Krauss, Tool Steels, ASM International, Materials Park, OH, 1998.

[66] J.C. Lippold, W.F. Savage, Solidification of austenitic stainless steel weldments: part III–the effect of solidification behavior on hot cracking susceptibility, Weld. J. 61 (1982) 388.

[67] E. Folkhard, Metallurgie der Schweißung nichtrostender Stähle, Springer-Verlag, Wien, Austria, 1984.

[68] M. Wolf, H. Schobbert, T. Böllinghaus, Influence of the weld pool geometry on solidification crack formation, in: A.J. Ramirez, J.C. Lippold (Eds.), Hot Cracking Phenomena in Welds, Springer, Berlin, Germany, 2005, pp. 245–268.

[69] H.J. Niu, I.T.H. Chang, Selective laser sintering of gas atomized M2 high speed steel powder, J. Mater. Sci. 35 (2000) 31–38.

[70] C.S. Wright, M. Youseffi, S.P. Akhtar, T.H.C. Childs, C. Hauser, P. Fox, Selective laser melting of prealloyed high alloy steel powder beds, Mater. Sci. Forum 514 (2006) 516–523 -516.

[71] Z.H. Liu, D.Q. Zhang, C.K. Chua, K.F. Leong, Crystal structure analysis of M2 high speed steel parts produced by selective laser melting, Mater. Charact. 84 (2013) 72–80.

[72] J. Sander, J. Hufenbach, M. Bleckmann, L. Giebeler, H. Wendrock, S. Oswald, T. Gemming, et al., Selective laser melting of ultra-high-strength TRIP steel: processing, microstructure, and properties, J. Mater. Sci. 52 (2017) 4944–4956.

[73] L. Wu, S. Das, W. Gridin, S. Leuders, M. Kahlert, M. Vollmer, T. Niendorf, Hot work tool steel processed by laser powder bed fusion: a review on most relevant influencing factors, Adv. Eng. Mater. 63 (2021) 2100049.

[74] J. Platl, H. Leitner, C. Turk, R. Schnitzer, Determination of martensite start temperature of high-speed steels based on thermodynamic calculations, Steel Res. Int. 91 (2020) 2000063.

[75] Z.H. Liu, C.K. Chua, K.F. Leong, K. Kempen, L. Thijs, E. Yasa, J. Van-Humbeeck, et al., A preliminary investigation on selective laser melting of M2 high speed steel, in: Proceedings of the 5th International Conference on Advanced Research and Rapid Prototyping, Leiria, Portugal, 2012, pp. 339–346.

[76] S. Karagöz, I. Liem, E. Bischoff, H.F. Fischmeister, Determination of carbide and matrix compositions in high-speed steels by analytical electron microscopy, Metall. Trans. A 20 (1989) 2695–2701.

[77] H. Fredriksson, M. Hillert, M. Nica, The decomposition of the M_2C carbide in high speed steel, Scand. J. Metall. 8 (1979) 115–122.